Using Cross-Sectional Cathodoluminescence to Visualize Process-Induced Defects in GaN-Based High Electron Mobility Transistors

RYUICHI SUGIE [1,2] TOMOYUKI UCHIDA,[1] KOJI MATSUMURA,[1] and HIDEKI SAKO[1]

1.—Toray Research Center Inc., 3-3-7, Sonoyama, Otsu, Shiga 520-8567, Japan. 2.—e-mail: Ryuichi_Sugie@trc.toray.co.jp

We performed cross-sectional cathodoluminescence (CL) for gallium nitride (GaN)-based high electron mobility transistors (HEMTs) to investigate process-induced defects. The cross-sectional CL measurements at room temperature clearly show the intensity distribution for the 25 nm-thick AlGaN layer, even though it is very thin. We also observed that the intensities of the band-edge emissions from the AlGaN and GaN layers fall near the source and drain regions. Those intensity decays demonstrate that ion implantation at the source and drain regions generates many nonradiative recombination centers and that these defects are not eliminated even by activation annealing after ion implantation. We also observed that the intensity of yellow luminescence (YL) in the GaN layer drops not only at the source and drain regions, but also in deeper regions of the 1.4 μm-thick GaN layer. We consider diffusion of the implantation-generated defects and their interactions with point defects in this deep region, which are responsible for the YL, to be the mechanism responsible for the YL intensity decrease. Ion implantation and subsequent annealing not only activates the dopant atoms, but also changes the point defects, which may affect the device characteristics. These findings show that cross-sectional CL spectral mapping can visualize the process-induced defects in GaN HEMTs and can therefore be used for process optimization and failure analysis of these devices.

Key words: Cathodoluminescence, GaN, HEMT, point defects, ion implantation, diffusion

INTRODUCTION

Because of their superior device characteristics, gallium nitride (GaN)-based high electron mobility transistors (HEMTs) are key devices for next-generation wireless communications.[1–5] To increase their power density, system efficiency, and bandwidth, it is essential to improve device structure and material quality. Several degradation mechanisms have been proposed already, using the failure-analysis approach.[6–10] However, effective physical and chemical characterization tools—such as x-ray diffraction (XRD), photoluminescence (PL) imaging, and x-ray photoelectron spectroscopy (XPS)—have mainly been used to characterize wafers. Only a few physical-analysis tools can be used after device fabrication because of their lack of spatial or depth resolution. Transmission electron microscopy (TEM) and scanning transmission electron microscopy (STEM) do have high spatial resolution and are suitable for device characterization, and they are typically used in failure analysis for devices.

However, they are not always perfect tools, and point defects—which are often generated during device processing—are difficult to observe via conventional TEM measurements. Such defects generated during device fabrication—such as those produced by ion implantation, thermal annealing, or dry etching, which may lead to fatal degradations—are often ignored because of the lack of suitable characterization methods.

In this work, we focus on using cross-sectional cathodoluminescence (CL) to visualize process-induced defects in GaN HEMTs. This technique has many advantages that are suitable for the characterization of semiconductor devices.[11,12] Our objective is to show that the CL method is effective for visualizing process-induced defects and for failure analysis of GaN HEMTs and related devices. On the basis of intensity changes in defect-related luminescence and the formation energy and diffusion coefficients of point defects, we also discuss a possible mechanism for point-defect formation and evolution during device fabrication.

EXPERIMENTAL

The devices we used in this work are commercially available 100 W GaN HEMTs designed for 2.5 GHz operation. To confirm the structure of the devices, we performed cross-sectional scanning electron microscopy (SEM) and energy-dispersive x-ray spectroscopy (EDX) measurements before performing the CL analysis. Figure 1 shows a SEM image of the device used in this work. The sample structure is overlaid on the SEM image in this figure. The device was formed by growing a 25 nm-thick AlGaN epitaxial layer and a 1.4 μm-thick GaN epitaxial layer on a silicon carbide (SiC) substrate. Figure 2 shows the STEM–EDX line profiles of Al and Si near the source. The concentration of Si atoms is high only to a depth of about 150 nm below the AlGaN surface. The STEM–EDX measurements indicated that Si, which is an n-type dopant in GaN, was implanted at the source and drain regions. The detailed implantation energy is unknown; however, we estimate it to be 100 keV or less based on the STEM–EDX line profiles of Si. The devices may be thermally annealed to activate dopant Si atoms; however, we could not determine the precise annealing conditions, because we used

commercially available HEMTs, and these conditions are not disclosed. Possible process conditions for implantation and annealing are discussed in the Results and Discussion session. A contact metal layer was deposited onto the AlGaN epitaxial layer only near the source and drain regions to form ohmic contact there. A silicon nitride (SiN) layer among the metal electrodes is used for passivation of the layer surface. The metal structure near the gate electrode, which is generally called a "field plate," is used to relax the electric field on the drain side of the gate.

Figure 3a shows a cross-sectional bright-field (BF)-STEM image near the gate. A high-magnification high-angle annular dark-field (HAADF)-STEM image of the interface between the AlGaN and GaN layers is shown in Fig. 3b. HAADF-STEM is sensitive to variations in the atomic number, and the AlGaN and GaN layers are clearly distinguished by
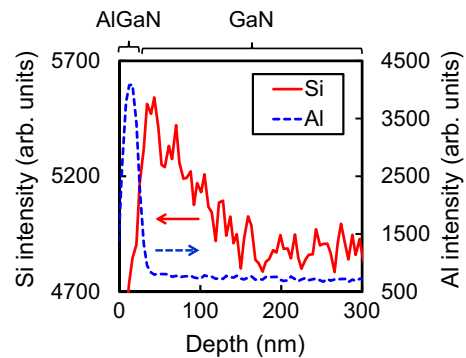

Fig. 2. STEM–EDX line profiles of Al and Si near the source.

Fig. 3. (a) Cross-sectional BF-STEM image near the gate. (b) High-magnification HAADF-STEM image at the interface between the GaN and AlGaN layers.
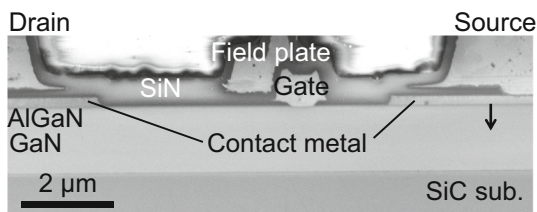

Fig. 1. Cross-sectional SEM image of the HEMT used in this work. The sample structure is overlaid on the SEM image. The black bold arrow near the source shows the position of the STEM–EDX measurement as indicated in Fig. 2.
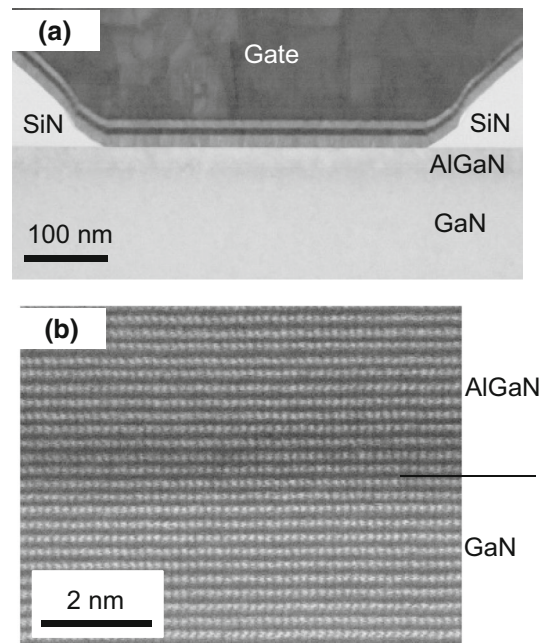
Using Cross-Sectional Cathodoluminescence to Visualize Process-Induced Defects in GaN-Based High Electron Mobility Transistors

5087

the contrast in the image. Figure 3b shows that the interface quality is excellent in this sample. The quality of the interface between the AlGaN and GaN layers may affect the device characteristics, because a two-dimensional electron gas (2DEG), which is the channel layer of the HEMT, is formed at the interface.

We also performed scanning capacitance microscopy (SCM) measurements to visualize the carrier distribution. We used a Bruker AXS NanoScope IVa for these SCM measurements. Figure 4 shows a differential-capacitance (dC/dV) image of the device. It can be seen that a 2DEG was formed at the interface between the AlGaN and GaN layers. The dC/dV signal is low near the source and drain regions as indicated by the white open ellipses in Fig. 4. The dC/dV output is not linear with carrier concentration because metallic or dielectric regions cannot be depleted and show no dC/dV signals.[13,14] Therefore, the regions indicated by white open ellipses in Fig. 4 have very low or high carrier concentrations. However, it is reasonable to suppose that these regions have very high concentrations, because they are the source and drain, and the dopant Si is also detected as shown in Fig. 2. Figure 4 also shows that the dC/dV signal is low at the gate. The reason for this is unknown at present; however, it suggests some kind of process-induced damage during metal patterning by dry etching. The SCM image shows that the 2DEG channel layer and the source and drain contacts are successfully formed in the device.

For the CL measurements, a JEOL JSM-7100F/TTLS SEM was used as an excitation source. The emitted light was analyzed using a HORIBA fiber-optic CL detection system with an iHR-320 single monochromator equipped with a cooled charge-coupled device (CCD). We recorded all spectra by scanning the electron beam in steps of 50–100 nm, and we constructed the CL intensity images from each spectrum afterward. We set the beam energy of the excitation electrons to 4 keV, for which the penetration depth is about 110–140 nm for GaN, based on several reported calculations.[15–17] We performed all CL measurements at room temperature. Low-temperature measurements are effective for luminescence techniques, because emissions become sharp and nonradiative recombination can be reduced. However, we chose room temperature measurements in this work because we need to visualize the nonradiative recombination centers generated during device fabrication.

RESULTS AND DISCUSSION

We applied the CL spectral-mapping measurements to the same sample we used for the SCM measurements. Figure 5 shows the panchromatic CL intensity image, and Fig. 6 shows the typical CL spectra of the AlGaN and the GaN layers at the positions indicated by 1, 2, and 3 in Fig. 5. The spectra of the GaN layers show a sharp emission at 364 nm and a broad band at around 400–700 nm. The former is a band-edge emission from GaN, and the latter is a defect-related emission, so-called yellow luminescence (YL).[18] The spectrum of the AlGaN layer shows a sharp emission at 320 nm in addition to the GaN band-edge emission. The emission at 320 nm is the AlGaN band-edge emission. The GaN band-edge emission is observed even at the AlGaN layer because of the restriction of the spatial resolution of the CL measurements. We estimate the Al composition ratio in the AlGaN layer to be 0.24, assuming a bowing parameter $C = 1.0$ eV.[19] However, there have been many values reported for the bowing parameter of AlGaN, ranging from $C = 0.53$ eV[20] to $C = 1.5$ eV.[21] The Al composition ratio ranges from 0.20 to 0.28, depending upon the chosen value of the bowing parameter.

In Fig. 5, the intensities near the source and drain regions are low. These regions are highly doped by the implantation of Si atoms to form the ohmic contacts, as discussed in the Experimental section. The decrease in intensity shows that ion implantation generates many nonradiative recombination centers and that the damage that it causes is not fully recovered even after activation annealing following ion implantation. Figure 5 also shows a slight intensity drop near the gate. The reason for this is unknown at present; however, the dC/dV signal is also weak near the gate, indicating some kind of process-induced damage.
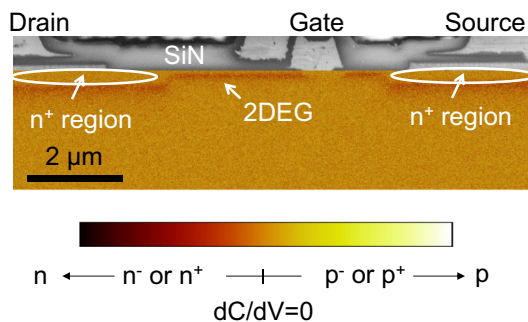

Fig. 4. SCM image of the HEMT. The SEM image of the metal electrodes is overlaid on the SCM image.
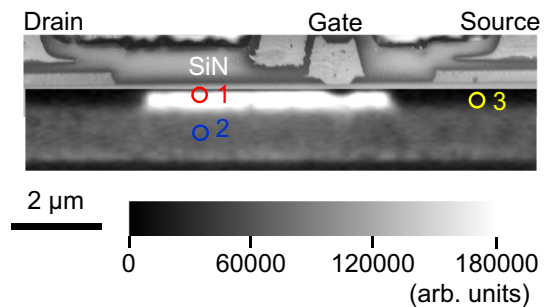

Fig. 5. Panchromatic CL intensity image of the HEMT. Open circles labelled 1, 2 and 3 show the positions of CL spectra indicated in Fig. 6.
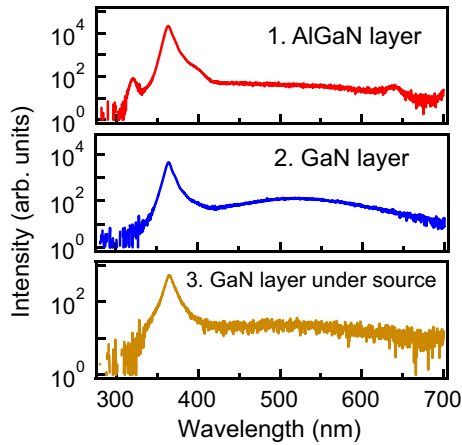
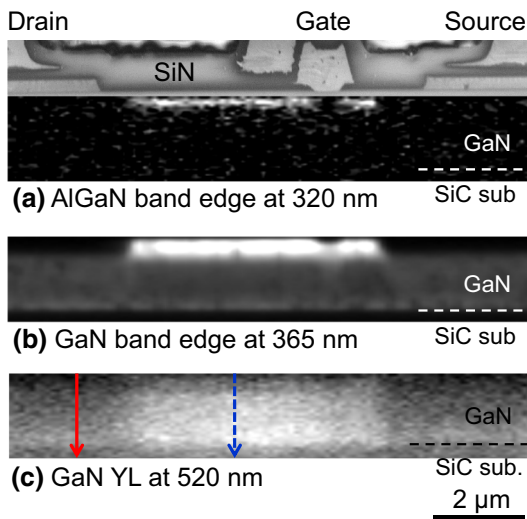Fig. 6. CL spectra at the positions labeled 1, 2, and 3 in Fig. 5.

Fig. 7. Monochromatic CL intensity images of (a) the AlGaN band edge, (b) the GaN band edge, and (c) the GaN yellow luminescence (YL). The solid red line and the dashed blue line show the sampling positions represented in Fig. 8.
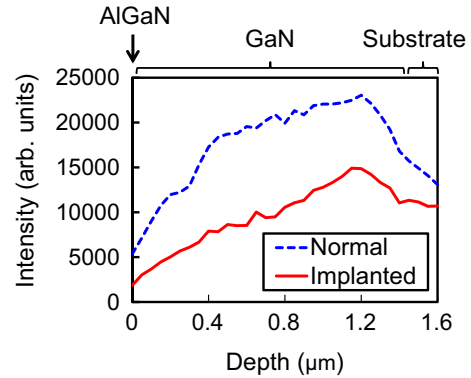

Fig. 8. The YL-intensity profile as a function of depth. The data are measured along the lines indicated in Fig. 7c. Note that the YL signal at 1.4–1.6 μm is meaningless because these regions are not the GaN layer but the SiC substrate.

Figures 7 show monochromatic CL intensity images of (a) the AlGaN band edge, (b) the GaN band edge, and (c) the GaN YL. These images provide more detailed information about the crystal defects in each layer. The intensity distribution from the AlGaN layer is clearly evident in Fig. 7a, even though the layer is very thin, and the generated carriers can easily diffuse into the GaN layer because of the band offset between AlGaN and GaN. In Fig. 7a and b, the intensities near the source and drain regions are low. This indicates that damage exists not only in the GaN layer, but also in the AlGaN layer. Figure 7b also shows that the band-edge emission of GaN is high just beneath the AlGaN layer between the drain and source regions. In general, the intensity of the band-edge emission is affected by the carrier concentration and the number of nonradiative recombination centers. This intensity change suggests that the epitaxial conditions of the GaN layer, such as growth rate, gas pressure, and temperature, may change during epitaxial growth, and the number of nonradiative recombination centers may differ. Another explanation is an effect of 2DEG formation. However, we could not identify the true cause of the intensity increase because detailed epitaxial conditions are unknown. In the image of the GaN YL in Fig. 7c, the intensity is not uniform, and it decreases under the source and drain regions, even if the intensity of the GaN band edge does not change much in the same regions. Figure 8 shows the YL intensity profiles measured along the lines indicated in Fig. 7c. The intensity of the implanted region drops to about half that of the normal region. Note that the YL signal at a depth of 1.4–1.6 μm is meaningless, because these regions are not the GaN layer but the SiC substrate. We simply derived intensity at 520 nm from each spectral mapping dataset when constructing the GaN YL map, and the defect-related emission from the SiC substrate also shows the intensity around 520 nm.

The drop in intensity under the source and drain regions does not originate from the epitaxial process that formed the GaN layer but from the device-fabrication process, because the dark regions coincide precisely with the implanted source and drain regions. This appears to be the result of direct interactions between the dopant Si atoms introduced by ion implantation and the defects responsible for the YL. However, the dopant Si atoms cannot interact directly with defects in the deeper regions of the 1.4 μm-thick GaN layer. Contact implantation is typically done at energy of 100 keV or less,[22–26] and SRIM calculations show that the maximum concentration of Si atoms is located within 150 nm of the surface.[27] In general, diffusion of the implanted atoms may occur after high-temperature thermal annealing. However, the diffusion of the Si atoms is negligible, because the diffusion coefficient of Si in GaN is low, and the concentration profile is almost preserved, even after high-temperature annealing.[22,25,28,29] Our STEM–

Using Cross-Sectional Cathodoluminescence to Visualize Process-Induced Defects
in GaN-Based High Electron Mobility Transistors

5089

EDX measurements also show that the concentration of Si atoms is high only within a depth of about 150 nm below the surface, as shown in Fig. 2. Therefore, the dopant Si atoms themselves cannot be the main cause of the decrease in YL intensity.

There are many types of native point defects in GaN, such as vacancies (V_{Ga}, V_N), self-interstitials (Ga_i, N_i), antisites (Ga_N, N_{Ga}), and their complexes. According to first-principles density-functional pseudopotential calculations, the vacancies have relatively low formation energies, and gallium vacancies (V_{Ga}) may be the dominant type of native point defect in n-type and unintentionally doped epitaxial films.[18,30] The self-interstitials and antisites have high formation energies, and are unlikely to occur during crystal growth because of the large size difference and the small bond length between the Ga and N atoms.[18,30,31] However, ion implantation easily generates interstitials and antisites, as well as vacancies. Thermal annealing after ion implantation also changes the defect conditions. The aim of thermal annealing is to move the dopant atoms into the expected substitutional sites and eliminate implantation-generated defects. Adequate annealing can annihilate the defects completely; however, the annealing temperature is not sufficient for most wide-bandgap semiconductors, which require quite high temperatures. Moderate annealing does not simply eliminate the defects, but extends them, and changes the defect configurations. Moreover, the defects can diffuse into deeper regions. The implantation-generated defects can interact with the native defects in the epitaxial layer during thermal annealing. The defect responsible for the YL can also be changed by interactions with the implantation-generated defects.

The origin of the YL has been somewhat controversial, and there seems to be no consensus on this issue at present. Many papers have speculated that the gallium vacancies (V_{Ga}) or V_{Ga} and their complexes with impurities may be responsible for the YL.[32–37] However, modern density-functional calculations and several experimental results show that carbon in nitrogen sites (C_N) or C_N and the complexes they form with other impurities are also possible candidates for the origin of the YL.[38–42] The diffusion coefficients of self-interstitials (Ga_i, N_i) are higher than those of carbon and oxygen impurities and of antisite defects (Ga_N, N_{Ga}), because the bond strengths of interstitials are relatively weak,[43] and they can easily combine with the vacancies. The detailed mechanism responsible for the intensity drop of the YL in a GaN HEMT is not fully understood at present; however, the decrease in YL intensity can be well explained if vacancy-type native point defects such as V_{Ga} or V_{Ga} and their complexes are responsible for the YL and if interactions between the implantation-generated interstitials and vacancy-type native point defects are dominant. One possible mechanism is as follows:

1. The implantation of dopant Si atoms creates many types of native point defects such as vacancies (V_{Ga}, V_N), self-interstitials (Ga_i, N_i), antisite defects (Ga_N, N_{Ga}), and their complexes.
2. Thermal annealing can activate the dopant Si atoms and eliminate the point defects generated. However, annealing does not simply eliminate the defects; it extends them and changes their configurations. Some defects—like self-interstitials—can diffuse into deeper regions.
3. The defects responsible for the YL can interact with the diffused defects, causing the YL intensity to decrease.

The intensity drop of the YL indicates that ion implantation and subsequent annealing not only activates the dopant atoms, but also changes the point defects, and may change the carrier lifetime and mobility. The cross-sectional CL spectral-mapping techniques can thus successfully visualize process-induced defects in GaN HEMTs and can therefore be used for process optimization and for failure analysis of GaN-based devices.

CONCLUSIONS

We performed cross-sectional CL for a GaN HEMT to investigate process-induced defects. The intensity distribution from the 25 nm-thick AlGaN layer is clearly evident, even though the layer is very thin. Moreover, we observed decreases in the CL intensities of the band-edge emissions from the AlGaN and GaN layers near the source and drain regions, which were generated by ion implantation to form ohmic contacts. The drop in intensity suggests that ion implantation generates many nonradiative recombination centers and demonstrates that the damage it causes is not fully recovered even after activation annealing following ion implantation. We also observed that the YL intensity was not uniform and that it decreased far from the source and drain regions. The intensity drop of the YL indicates that ion implantation and subsequent annealing not only activates the dopant atoms but can also change the point defects. The origin of the YL has not been fully identified at this time; however, the intensity decrease can be well explained if vacancy-type native point defects are responsible for the YL and the diffused implantation-generated interstitials interact with those vacancy-type defects. We conclude that cross-sectional, high-speed CL spectral mapping can be used to visualize process-induced defects in GaN HEMTs and can thus be used for process optimization and failure analysis of GaN-based devices.

CONFLICT OF INTEREST

The authors declare that they have no conflict of interest.

REFERENCES

1. B.J. Baliga, *Semicond. Sci. Technol.* 28, 074011 (2013).
2. H. Amano, Y. Baines, E. Beam, M. Borga, T. Bouchet, P.R. Chalker, M. Charles, K.J. Chen, N. Chowdhury, R. Chu, C. De Santi, M. Merlyne De Souza, S. Decoutere, L. Di Cioccio, B. Eckardt, T. Egawa, P. Fay, J.J. Freedsman, L. Guido, O. Häberlen, G. Haynes, T. Heckel, D. Hemakumara, P. Houston, J. Hu, M. Hua, Q. Huang, A. Huang, S. Jiang, H. Kawai, D. Kinzer, M. Kuball, A. Kumar, K.B. Lee, X. Li, D. Marcon, M. März, R. McCarthy, G. Meneghesso, M. Meneghini, E. Morvan, A. Nakajima, E.M.S. Narayanan, S. Oliver, T. Palacios, D. Piedra, M. Plissonnier, R. Reddy, M. Sun, I. Thayne, A. Torres, N. Trivellin, V. Unni, M.J. Uren, M. Van Hove, D.J. Wallis, J. Wang, J. Xie, S. Yagi, S. Yang, C. Youtsey, R. Yu, E. Zanoni, S. Zeltner, and Y. Zhang, *J. Phys. D Appl. Phys.* 51, 163001 (2018).
3. B.M. Green, K.K. Chu, E.M. Chumbes, J.A. Smart, J.R. Shealy, and L.F. Eastman, *IEEE Electron Device Lett.* 21, 268 (2000).
4. U.K. Mishra, P. Parikh, and Y.F. Wu, *Proc. IEEE* 90, 1022 (2002).
5. R.S. Pengelly, S.M. Wood, J.W. Milligan, S.T. Sheppard, and W.L. Pribble, *IEEE Trans. Microw. Theory Tech.* 60, 1764 (2012).
6. J. Kuzmik, G. Pozzovivo, C. Ostermaier, G. Strasser, D. Pogany, E. Gornik, J.-F. Carlin, M. Gonschorek, E. Feltin, and N. Grandjean, *J. Appl. Phys.* 106, 124503 (2009).
7. M. Baeumler, F. Gütle, V. Polyakov, M. Cäsar, M. Dammann, H. Konstanzer, W. Pletschen, W. Bronner, R. Quay, P. Waltereit, M. Mikulla, O. Ambacher, F. Bourgeois, R. Behtash, K.J. Riepe, P.J. van der Wel, J. Klappe, and T. Rödle, *J. Electron. Mater.* 39, 756 (2010).
8. M. Montes Bajo, C. Hodges, M.J. Uren, and M. Kuball, *Appl. Phys. Lett.* 101, 033508 (2012).
9. G. Meneghesso, M. Meneghini, and E. Zanoni, *Jpn. J. Appl. Phys.* 53, 100211 (2014).
10. F. Berthet, S. Petitdidier, Y. Guhe, J.L. Trolet, P. Mary, A. Vivier, C. Gaquière, and B. Boudart, *Solid State Electr.* 127, 13 (2017).
11. R. Sugie, T. Mitani, M. Yoshikawa, Y. Iwata, and R. Satoh, *Jpn. J. Appl. Phys.* 49, 04DP15 (2010).
12. R. Sugie, T. Uchida, K. Kosaka, and K. Matsumura, *Jpn. J. Appl. Phys.* 55, 04ER03 (2016).
13. R. Stephenson, A. Verhulst, P. De Wolf, and M. Caymax, *Appl. Phys. Lett.* 73, 2597 (1998).
14. P. De Wolf, R. Stephenson, T. Trenkler, T. Clarysse, and T. Hantschel, *J. Vac. Sci. Technol., B* 18, 361 (2000).
15. K. Kanaya and S. Okayama, *J. Phys. D Appl. Phys.* 5, 43 (1972).
16. O. Kurniawan and V.K.S. Ong, *Scanning* 29, 280 (2007).
17. R. Sugie, T. Uchida, T. Fujii, and T. Araki, *Jpn. J. Appl. Phys.* 58, 010902 (2019).
18. M.A. Reshchikov and H. Morkoç, *J. Appl. Phys.* 97, 061301 (2005).
19. I. Vurgaftman and J.R. Meyer, *J. Appl. Phys.* 94, 3675 (2003).
20. H. Jiang, G.Y. Zhao, H. Ishikawa, T. Egawa, T. Jimbo, and M. Umeno, *J. Appl. Phys.* 89, 1046 (2001).
21. S.A. Nikishin, N.N. Faleev, A.S. Zubrilov, V.G. Antipov, and H. Temkin, *Appl. Phys. Lett.* 76, 3028 (2000).
22. S.O. Kucheyev, J.S. Williams, and S.J. Pearton, *Mater. Sci. Eng.* 33, 51 (2001).
23. H. Yu, L. McCarthy, S. Rajan, S. Keller, S. Denbaars, J. Speck, and U. Mishra, *IEEE Electron Device Lett.* 26, 283 (2005).
24. F. Recht, L. McCarthy, S. Rajan, A. Chakraborty, C. Poblenz, A. Corrion, J.S. Speck, and U.K. Mishra, *IEEE Electron Device Lett.* 27, 205 (2006).
25. T. Shiino, T. Saitoh, T. Nakamura, and T. Inada, *Nucl. Instr. Methods B* 267, 1571 (2009).
26. K. Nomoto, Y. Toyoda, M. Saitoh, T. Inada, and T. Nakamura, *Nucl. Instr. Methods B* 272, 125 (2012).
27. J.F. Ziegler, J.P. Biersack, and U. Littmark, *The Stopping and Range of Ions in Solids*, Vol. 1 (New York: Pergamon Press, 1984).
28. A.Y. Polyakov, M. Shin, M. Skowronski, R.G. Wilson, D.W. Greve, and S.J. Pearton, *Solid State Electron.* 41, 703 (1997).
29. A. Munkholm, G.B. Stephenson, J.A. Eastman, O. Auciello, M.V. Ramana Murty, C. Thompson, P. Fini, J.S. Speck, and S.P. DenBaars, *J. Cryst. Growth* 221, 98 (2000).
30. S. Limpijumnong and C.G. Van de Walle, *Phys. Rev. B* 69, 035207 (2004).
31. J. Neugebauer and C.G. Van de Walle, *J. Appl. Phys.* 85, 3003 (1999).
32. E. Calleja, F.J. Sánchez, D. Basak, M.A. Sánchez-García, E. Muñoz, I. Izpura, F. Calle, J.M.G. Tijero, J.L. Sánchez-Rojas, B. Beaumont, P. Lorenzini, and P. Gibart, *Phys. Rev. B* 55, 4689 (1997).
33. C.B. Soh, S.J. Chua, H.F. Lim, D.Z. Chi, S. Tripathy, and W. Liu, *J. Appl. Phys.* 96, 1341 (2004).
34. A. Sedhain, J. Li, J.Y. Lin, and H.X. Jiang, *Appl. Phys. Lett.* 96, 151902 (2010).
35. P. Kamyczek, E. Placzek-Popko, V. Kolkovsky, S. Grzanka, and R. Czernecki, *J. Appl. Phys.* 111, 113105 (2012).
36. S. Ito, T. Nakagita, N. Sawaki, H.S. Ahn, M. Irie, T. Hikosaka, Y. Honda, M. Yamaguchi, and H. Amano, *Jpn. J. Appl. Phys.* 53, 11RC02 (2014).
37. M. Julkarnain, N. Kamata, T. Fukuda, and Y. Arakawa, *Opt. Mater.* 60, 481 (2016).
38. J.L. Lyons, A. Janotti, and C.G. Van de Walle, *Appl. Phys. Lett.* 97, 152108 (2010).
39. D.O. Demchenko, I.C. Diallo, and M.A. Reshchikov, *Phys. Rev. Lett.* 110, 087404 (2013).
40. M.A. Reshchikov, D.O. Demchenko, A. Usikov, H. Helava, and Yu Makarov, *Phys. Rev. B* 90, 235203 (2014).
41. S.G. Christenson, W. Xie, Y.Y. Sun, and S.B. Zhang, *J. Appl. Phys.* 118, 135708 (2015).
42. M.A. Reshchikov, J.D. McNamara, F. Zhang, M. Monavarian, A. Usikov, H. Helava, Yu Makarov, and H. Morkoç, *Phys. Rev. B* 94, 035201 (2016).
43. A. Kyrtsos, M. Matsubara, and E. Bellotti, *Phys. Rev. B* 93, 245201 (2016).